Nano Research

Open Access

Research Article

Stabilizing Co nanoparticles for CO_2 hydrogenation by lattice-matching confinement in ZnO interlayers

Wangxing Zhang[1], Yu Luo[1], Sónia A.C. Carabineiro[2], Shuai Lyu[1] ✉, Wenwen Xiao[1], Zhiyan He[1,3], Zhu'an Zheng[4], and Junjiang Zhu[1] ✉

[1] *Hubei Key Laboratory of Biomass Fibers and Eco-dyeing & Finishing, College of Chemistry and Chemical Engineering, Wuhan Textile University, Wuhan 430200, China*
[2] *LAQV-REQUIMTE, Department of Chemistry, NOVA School of Science and Technology, Universidade NOVA de Lisboa, 2829-516 Caparica, Portugal*
[3] *State Key Laboratory of Pulp and Paper Engineering, South China University of Technology, Guangzhou 510640, China*
[4] *School of Automotive Engineering, Yancheng Institute of Technology, Yancheng 224000, China*

Cite this article: *Nano Research*, **2025**, *18*, 94907282. https://doi.org/10.26599/NR.2025.94907282

ABSTRACT: Confining active nanoparticles within specific nanoscale spaces is a promising strategy to improve the catalytic activity, selectivity and stability of catalysts. In this study, we present a lattice-matching approach to confine Co particles within ZnO layers (ZnO/Co/ZnO) for CO_2 hydrogenation, a critical and challenging reaction in the field of CO_2 utilization and energy production. XRD patterns reveal that the lattice mismatch between ZnO and hexagonal wurtzite CoO (w-CoO) is only 0.18%, facilitating the epitaxial growth of w-CoO on the ZnO surface, or vice versa. This minimal mismatch enables the successful confinement of w-CoO within the ZnO interlayers. This advanced methodology can also be adapted to diverse ZnO morphologies, allowing the optimization of the confined catalyst microstructure. Significantly, when Co particles are confined within the interlayer of ZnO, they exhibit excellent catalytic activity, achieving a rate of 15.8 $\mu mol_{CO_2} \cdot g_{Co}^{-1} \cdot s^{-1}$ for CO_2 hydrogenation reaction. Moreover, no appreciable deactivation was observed even after 700 h of continuous operation. These results introduce a novel approach for the development of confined catalysts with enhanced activity and long-term stability.

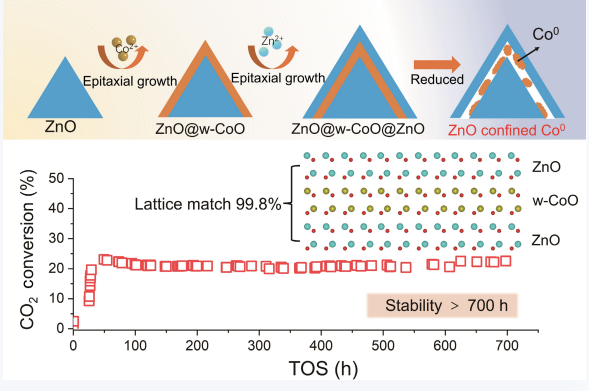

KEYWORDS: lattice-matching, epitaxial growth, confined catalyst, CO_2 hydrogenation, catalytic stability

1 Introduction

Space-confinement has emerged as a promising strategy for synthesizing highly efficient catalytic materials [1–3]. The physicochemical properties of confined catalysts can be significantly modified by their unique chemical microenvironments, altering the ability to react with substrates [4, 5], improving the selectivity to specific products [6, 7], and accelerating the reaction rates [8]. In particular, confined systems are expected to offer superior stability, as they prevent surface deterioration and particle aggregation [9].

Received: December 13, 2024; **Revised:** January 22, 2025
Accepted: February 3, 2025

✉Address correspondence to Shuai Lyu, shuailyu@wtu.edu.cn; Junjiang Zhu, jjzhu@wtu.edu.cn

For example, the interior space of carbon nanotubes (CNTs) provides a uniquely confined environment for hosting active nanoparticles [10]. Pan et al. demonstrated that the catalytic activity of a bicomponent RhMn catalyst for syngas (a mixture of CO and H_2) conversion to C_2 oxygenates was significantly enhanced when located within the CNTs channels compared to being outside. This enhancement was attributed to the increased local concentration of reactants in the confined spaces of the CNTs [11]. Furthermore, CO was more enriched relative to H_2 due to its stronger interaction with the CNTs interior surface, resulting in a CO/H_2 ratio higher than that of the bulk syngas feed. This shift in reaction ratio led to modified product selectivities [12]. The channels of CNTs also impose spatial confinement on metal particles, effectively preventing their aggregation under reaction conditions. For instance, the interior Fe_xC particles retained size in the range of 6–11 nm, while exterior particles grew significantly, with the largest reaching 24 nm after 125 h of Fischer–Tropsch synthesis [13].

Beyond CNTs, a variety of other porous materials also provide confined spaces that can enhance the performance of embedded nanoparticles [14].

The conventional approach to design nano-confined catalysts typically begins with the preparation of a support that incorporates a tailored pore structure. This is followed by the impregnation of metal salt into these pores using a solution method. Finally, the metal salt precursors are converted into oxide particles through a calcination process. However, this commonly employed method encounters some challenges. For example, precise modification of the inner surface of the support material is essential to prevent particle deposition on the outer surface of the confined space and ensure that the majority of the metal salt precursors infiltrate into the pores [15]. Additionally, during high-temperature calcination, particle agglomeration or migration towards the exterior of pores can occur. Thus, developing innovative methodologies for the precise regulation of the fine structure in confined catalysts is of great significance.

Using atomic layer deposition technology, Qin et al. successfully constructed an Al_2O_3 confined Ni catalyst through a layer-by-layer deposition process [16]. Inspired by this approach, we attempt to utilize the ultra-high matching properties in the lattice of ZnO and hexagonal wurtzite CoO (w-CoO) to design confined materials in this work. Epitaxial seeded growth is a highly effective strategy for the wet-chemical synthesis of hybrid nanomaterials [17]. The lattice mismatch (f) plays a crucial role in determining the mode of epitaxial growth. When the lattice mismatch between two oxides is less than 5%, one oxide can grow epitaxially on the surface of the other, forming a continuous coating layer rather than dispersed nanoparticles, in line with the Frank-van der Merwe (FM) model [18]. It is reported that ZnO and w-CoO share identical crystal structures, with a lattice mismatch value of only 0.18% [19]. This small mismatch significantly promotes the epitaxial growth of one oxide on the surface of the other, leading to the formation of a continuous coating layer. By alternating growth of two oxides, it is possible to create a multilayer structure where one component is confined by the other (Fig. S1 in the Electronic Supplementary Material (ESM)). Additionally, utilizing the lattice mismatch strategy provides precise control over the microstructure of the confined catalyst, enabling fine-tuned regulation of its properties for enhanced catalytic performance.

2 Results and discussion

2.1 Design of the confined catalyst

The powder X-ray diffraction (XRD) comparison between pure ZnO and w-CoO is illustrated in Fig. 1(a). The XRD peaks of the two components are nearly identical, exhibiting a lattice mismatch of only 0.18%, as shown in Fig. 1(b) and Table S1 in the ESM. On this basis, we attempt to grow w-CoO on the surface of ZnO to synthesize ZnO@w-CoO-P (Z@C-P, where P represents a pyramid morphology), which then used as a heteronucleus for the growth of an additional ZnO layer, in order to effectively confine w-CoO within the ZnO matrix, i.e., ZnO@w-CoO@ZnO-P (Z@C@Z-P). This material is finally treated by H_2 reduction, to transform the w-CoO in the inner layer into Co^0 particles (Fig. 1(c)). Scanning transmission electron microscopy (STEM) and the corresponding energy dispersive X-ray spectrum (EDX) analysis reveal that the as-synthesized Z@C-P nanoparticles are highly uniform with an average size of 47.6 nm (Fig. 1(d)), and the surface of ZnO particles is coated with a w-CoO layer (Fig. 1(e)). The side view of a single Z@C-P nanoparticle reveals that it has a triangular shape, while the top view shows a hexagonal morphology. This implies that the Z@C-P nanoparticle exhibits a hexagonal pyramidal shape characteristic of anisotropic growth (Figs. 1(f)–1(i)) [20].

STEM and EDX mapping techniques are also employed to determine the particle size, morphology and element distribution of the Z@C@Z-P material. As shown in (Figs. 1(j) and 1(k)), the particle size of Z@C@Z-P is approximately 61.3 nm, displaying a distinctive sandwich structure. The outer surface of the particles is uniformly coated with ZnO. Characterizing a single particle from multiple perspectives offers deeper insights into the microstructure of the Z@C@Z-P material, which reveals that CoO is confined within the ZnO layers, and the particles remain the hexagonal pyramidal morphology (Figs. 1(l)–1(o)).

The reduced Z@C@Z-P catalyst was comprehensively characterized, revealing that the reduced particles partially preserved their original morphology (Fig. S2 in the ESM), with Co localized within the inner layer of ZnO. No characteristic diffraction peaks of metallic Co were observed in the XRD pattern of the reduced catalyst (Fig. S3 in the ESM), indicating that only a small fraction of CoO was reduced, while the majority of cobalt species remained in the form of oxides. ZnO is commonly used as a support for CO_2 hydrogenation. It remains relatively stable when the pretreatment temperature of hydrogen is kept below 450 °C [21].

2.2 Structural regulation of the confined catalyst

The Co content within the ZnO layer can be readily adjusted using this advanced approach, through modulating the amount of Co precursors during synthesis. The XRD patterns of the Z@C-P materials are shown in Fig. S4 in the ESM, displaying typical hexagonal diffraction peaks that align closely with these of the standard ZnO card. No distinctive diffraction peaks corresponding to other Co oxide species are observed, indicating the presence of w-CoO, which overlaps with the characteristic diffraction peaks of ZnO. The EDX-mapping and inductively coupled plasma optical emission spectrometry (ICP-OES) data for Z@C-P with varying Co contents are presented in Fig. S5 and Table S2 in the ESM, respectively. At a Co loading of 3.7%, only a small amount of Co is distributed on the surface of ZnO (Fig. S5(a) in ESM). As the loading increases, Co gradually forms a coating layer on the outer surface of ZnO. When the Co loading reaches 31.6%, there is a notable increase in the coating thickness (Fig. S5(c) in ESM).

The Z@C@Z-P materials, with varying Co loading, are then synthesized using the Z@C-P samples as heterogeneous seed. Figure 2(a) illustrates the XRD pattern of the materials, which shows that they all exhibit well-matched characteristic diffraction peaks to these of ZnO, indicating the absence of any other crystalline species. The Co loading in Z@C@Z-P ranges from 1.5% to 25.6% (Fig. 2(b) and Table S2 in ESM). The nitrogen absorption-desorption analysis reveals that both the Z@C-P and Z@C@Z-P nanoparticles exhibit a H3 type hysteresis loop, indicating the presence of internal holes rather than pores due to particle accumulations. The surface areas of the materials are 19.3 and 31.5 $m^2 \cdot g^{-1}$, respectively, which indicates that the coating of ZnO can enhance the surface area of the Z@C-P material (Fig. 2(c)).

The morphology and elemental distribution of individual particles in Z@C@Z-P materials are further characterized with STEM-EDX measurement, to provide detailed structural

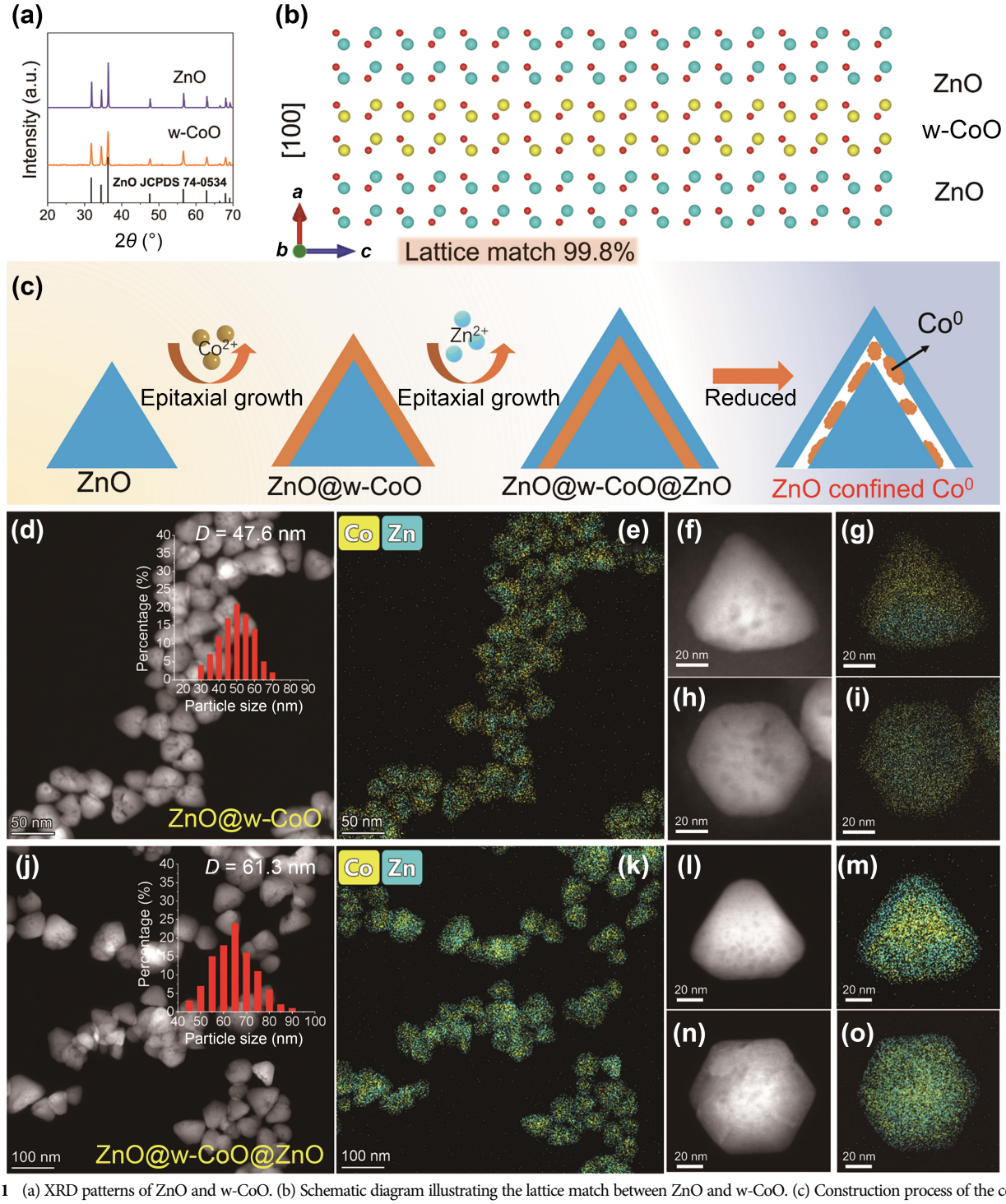

Figure 1 (a) XRD patterns of ZnO and w-CoO. (b) Schematic diagram illustrating the lattice match between ZnO and w-CoO. (c) Construction process of the confined catalyst based on the lattice match mechanism. (d) STEM image and (e) corresponding EDX mapping of the Z@C-P material. (f)–(i) STEM images and corresponding EDX mappings of a single Zn@C-P nanoparticle from different angles. (j) STEM image and (k) corresponding EDX mapping of the Z@C@Z-P material. (l)–(o) STEM images and corresponding EDX mappings of a single Z@C@Z-P nanoparticle from different angles.

information. Side-view STEM images of the Z@C@Z-P materials, along with their corresponding elemental distribution, are presented in Figs. 2(d)–2(f). All the samples exhibit regular triangular shapes in the side view, while appearing hexagonal in the bottom view (Fig. S6 in the ESM). As shown in Figs. 2(d2)–2(f2), there is a noticeable confined space inside the particles that gradually increases with the Co loading.

Interestingly, the particles exhibit a high density of surface voids, with size ranging from 5 to 8 nm, as observed from the STEM images (Fig. S7 in the ESM). These voids arise from localized uneven growth during nanoparticle formation. These openings can serve as contact channels between w-CoO and the reactants. Additionally, we observed that epitaxial growth is infrequent at the base of the pyramid. This phenomenon can be attributed to the fact that the base of the pyramid predominantly exposes its {001} surface. The {001} plane of ZnO terminates with either O^{2-} or Zn^{2+}

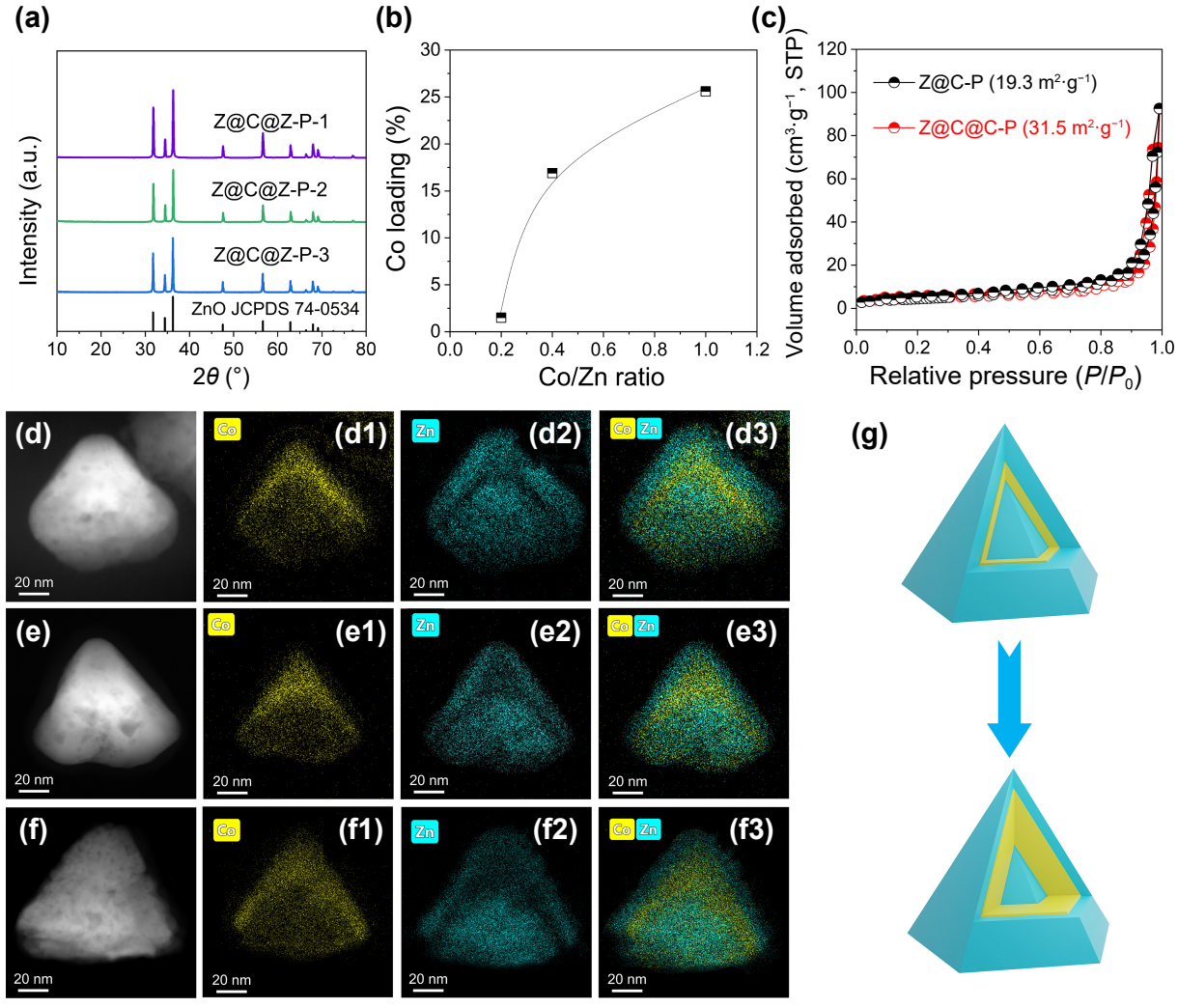

Figure 2 (a) XRD patterns of different Z@C@Z-P materials. (b) Effect of Co loading on Z@C@Z-P materials with varying Co/Zn molar ratios of the precursor. (c) N_2 physisorption isotherms of the Z@C-P and Z@C@Z-P catalyst. (d)–(f) STEM images and corresponding EDX mappings of Z@C@Z-P-1, Z@C@Z-P-2 and Z@C@Z-P-3 from a side-view, respectively. (g) Schematic diagram illustrating the regulation of Co in confined spaces.

ions. During the growth process, the Zn ligand monomer may have reduced accessibility to the ZnO surface when it terminates with O^{2-} [22]. Moreover, the presence of hydroxyl groups on the Zn^{2+} surface can impede ZnO growth, causing the CoO on this crystal facet to interact more with the surrounding environment rather than being fully encapsulated by ZnO [23, 24]. These factors together reduce the frequency of epitaxial growth at the base. Overall, the lattice matching approach proves effective in regulating the Co content within a confined space, as shown in Fig. 2(g).

As previously noted, the precise regulation of confined nanomaterial structures presents a significant challenge. ZnO is a remarkable material recognized for its sensitivity to crystal surface properties and its controllable morphology [25]. Among its typical forms, rod-like ZnO features six {100} facets exposed on the sides and two {002} facets at the bottom [26]. In this study, we found that the confined catalyst can also be obtained using rod-like ZnO as substrate through the lattice match strategy. The ZnO@w-CoO-R material (Z@C-R, where R represents a rod morphology) also displays characteristic hexagonal diffraction peaks that closely match those of pure ZnO (Fig. S8 in the ESM). The EDX mappings of Z@C-R, coated with varied w-CoO thicknesses, are shown in Fig. S9 in the ESM. It is evident that the thickness of the epitaxial layer can be successfully controlled by adjusting the concentration of the Co precursor, resulting in thicknesses of 12, 28 and 46 nm at Co loading of 4.7%, 15.3% and 20.9%, respectively (Table S3 in the ESM).

Similarly, The Co content in the ZnO@w-CoO@ZnO-R catalyst (Z@C@Z-R) can also be regulated, without destroying the matrix structure (Figs. S10–S12 in the ESM), indicating that the lattice match method for creating confined catalysts can be extended to ZnO with other morphologies. This offers a promising avenue to precisely manipulate the localized microstructure of confined catalysts.

2.3 CO_2 hydrogenation performance

The CO_2 hydrogenation catalyst is evaluated in a fixed bed reactor. Before the catalytic performance test, the catalyst is reduced in a H_2 atmosphere at 300 °C for 3 h. Pure Co_3O_4 and Co_3O_4/ZnO catalyst were used for comparison. The results are presented in Fig. 3 and Table S4 in the ESM. ZnO exhibits negligible activity for CO_2 hydrogenation even at 250 °C. It can be seen that the Co_3O_4 catalyst achieves a CO_2 conversion rate of 36% and exhibits a CH_4 selectivity as high as 98%. The CO_2 conversion of Co_3O_4/ZnO catalyst is 26.1%, with CH_4 being the predominant product.

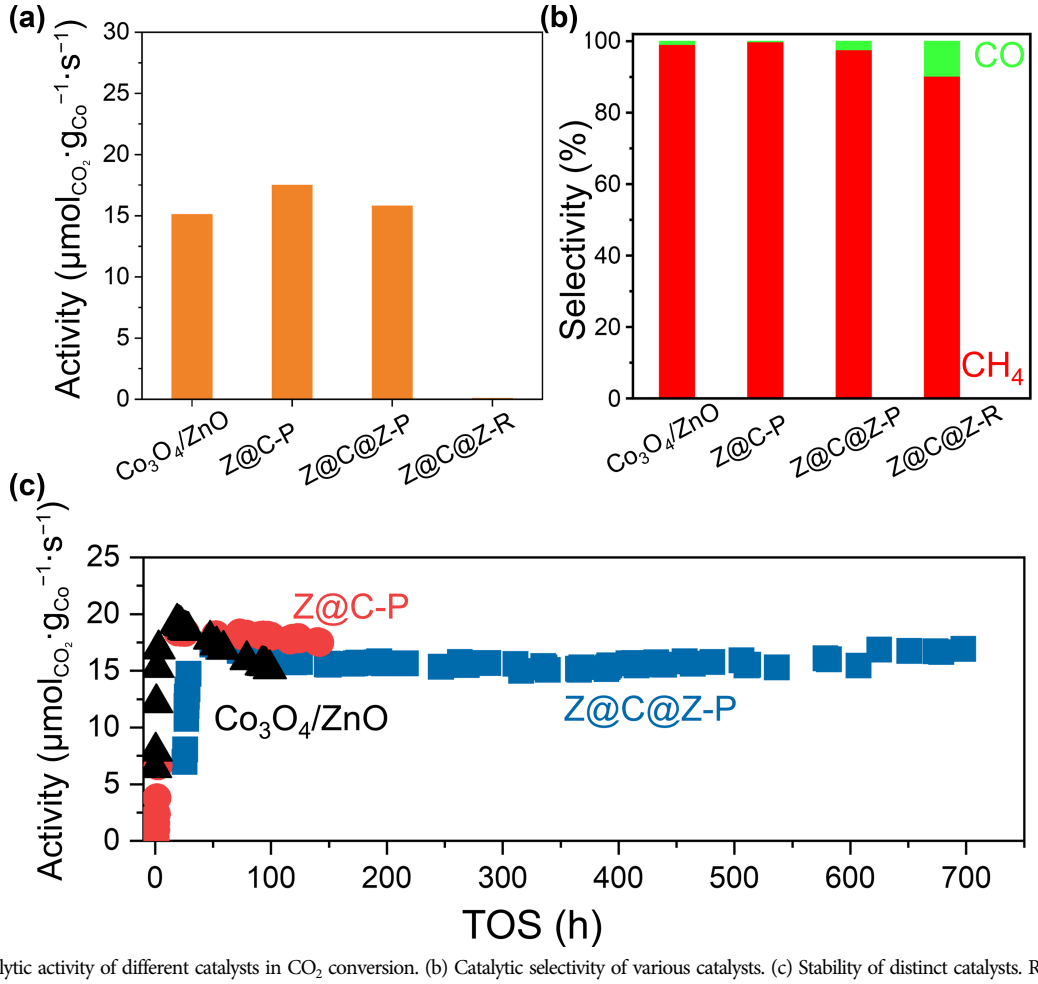

Figure 3 (a) Catalytic activity of different catalysts in CO_2 conversion. (b) Catalytic selectivity of various catalysts. (c) Stability of distinct catalysts. Reaction conditions: T = 250 °C, P = 2.0 MPa, GHSV = 6 L·s^{-1}·g$_{cat}^{-1}$, $H_2/CO_2/N_2$ = 67.5%/22.5%/10%.

Considering that ZnO alone does not contribute to the reaction, the CO_2 conversion observed on Co_3O_4/ZnO comes mainly from the Co active sites (reduced from Co_3O_4). For this, the cobalt time yield (CTY), representing the amount of CO_2 converted per gram of Co particles, is calculated to be 15.1 μmol$_{CO_2}$·g$_{Co}^{-1}$·s^{-1} at 250 °C. The CTY value increases to 17.5 μmol$_{CO_2}$·g$_{Co}^{-1}$·s^{-1} over the Z@C-P as catalyst, demonstrating that the material prepared by the lattice-matching method is more favorable for the reaction. In contrast, the confined Z@C@Z-P catalyst exhibits a CO_2 conversion of 21.5% and a CTY value of 15.8 μmol$_{CO_2}$·g$_{Co}^{-1}$·s^{-1} (Fig. 3(a)). Notably, the Z@C@Z-R catalyst (Co loading of 20.9%) displays extremely lower CO_2 conversion of 2.1% and higher CO selectivity.

2.4 The structure-activity relationship

The activity of Co-based catalysts for CO_2 hydrogenation is closely linked to their reducibility, and it is generally believed that Co^0 exhibits higher activity and CH_4 selectivity compared to CoO [27]. In this respect, we measure the reducibility of catalysts with H_2 temperature-programmed reduction (H_2-TPR). The reduction behavior of Co_3O_4 is characterized by a typical two-step process (Fig. S13 in the ESM). The reduction peak at 336 °C corresponds to the reduction of Co_3O_4 to CoO, while the peak at 459 °C is attributed to the reduction of CoO to Co^0 [28]. Notably, the reduction peaks for the Co_3O_4/ZnO catalyst occur at lower temperatures compared to pure Co_3O_4. Specifically, the reduction peak from Co_3O_4 to CoO shifts to 294 °C, and the peak from CoO to Co^0 shifts to 448 °C. For the Z@C-P catalyst, the peak at 249 °C is attributed to the reduction of Co^{3+} to Co^{2+} due to partial oxidation of the surface. The two broad peaks at lower temperatures (320 °C and 383 °C) are attributed to the reduction of surface and interface CoO to Co^0. In contrast, the reducibility of Z@C@Z-P is weakened, with the two reduction peaks occurring at 336 and 375 °C. The Z@C@Z-R, however, displays negligible reduction peaks below 700 °C, suggesting an extremely weak reducibility, which may account for its poor catalytic activity and higher CO selectivity. Experimental and theoretical studies demonstrate that the heterolytic cleavage of H_2 on ZnO forms highly reactive O–H and Zn–H species, which are prone to migration [29, 30]. The H species adsorbed on ZnO can migrate to the surface of Co_3O_4, thereby facilitating its reduction [31]. It is evident that the reduction peak of CoO to Co^0 in Z@C-P occurs at a lower temperature than in Co_3O_4/ZnO, suggesting a more pronounced hydrogen spillover effect in the Z@C-P catalyst.

The enhanced hydrogen spillover effect in the Z@C-P sample may be attributed to stronger interactions between ZnO and CoO, as evidenced by X-ray photoelectron spectroscopy (XPS) after reduction. Figure S14(a) in the ESM shows the Co 2p spectrum of the catalyst after reduction, where a Co^{2+} satellite peak at 786.7 eV and a distinct Co^0 peak at 778 eV are observed [32], indicating the coexistence of CoO and Co^0 species. Additionally, the characteristic diffraction peak attributed to Co^0 is visible in the XRD pattern of the reduced Z@C-P and Co_3O_4/ZnO catalyst. In contrast, no Co^0

diffraction peak was observed for the Z@C@Z-P and Z@C@Z-R catalyst (Fig. S15 in the ESM), indicating that only a small amount of Co was reduced in these catalysts. Upon examining the Zn 2p peak of the reduced catalyst, it is noted that the binding energy of the Co_3O_4/ZnO catalyst shifts by 0.2 eV towards higher values compared to the ZnO support (Fig. S14(b) in the ESM). This shift suggests an interaction between ZnO and Co species, with electron transfer from ZnO to Co^0 [31]. For the Z@C-P catalyst, the Zn peak shift is more pronounced, indicating a stronger interaction between ZnO and Co species. In the case of the Z@C@Z-P catalyst, the Zn 2p peak shifts by 0.7 eV relative to ZnO, further confirming the enhanced interaction between ZnO and Co, consistent with the H_2-TPR results. It has been reported that the work functions of ZnO (100) and CoO (111) surfaces are 5.04 and 6.14 eV, respectively. This suggests that during the reaction, electrons on the ZnO surface transfer to the Co^0 surface. The electron transfer accelerates the migration of H to Co and promoting their interaction with CH_x species to produce CH_4 [24].

Based on the H_2 temperature-programmed desorption (H_2-TPD, Table S5 in the ESM), the turnover frequency (TOF) of the catalysts was further calculated. It is evident that the TOF value for Z@C-P is 0.34 min^{-1}, which is higher than the 0.26 min^{-1} of the Co_3O_4/ZnO catalyst. In comparison, Z@C@Z-P exhibits the highest TOF value at 1.01 min^{-1}. This trend is closely associated with the interactions between the components of the catalysts. For the Z@C-P catalyst, the strong interaction between Co-Zn enhances the hydrogen spillover effect and facilitates electron transfer between the components, thereby increasing the intrinsic activity of the catalyst. In the case of the Z@C@Z-P catalyst, although the reducibility is not as high, the unique confined environment in the limited region may play a crucial role in promoting the reaction.

2.5 Catalytic stability of confined catalyst

The stability tests, conducted at 250 °C, demonstrate a decrease in the CO_2 CTY for Co_3O_4/ZnO, from 19.3 to 15.1 $\mu mol_{CO_2} \cdot g_{Co}^{-1} \cdot s^{-1}$, over a period of 100 h. In comparison, the CO_2 CTY of Z@C-P decreases from 18.4 to 17.5 $\mu mol_{CO_2} \cdot g_{Co}^{-1} \cdot s^{-1}$ over 140 h (Fig. 3(b)), indicating a better stability due to the close contact between CoO and ZnO. Notably, the Z@C@Z-P exhibits exceptional stability, maintaining its performance for an extended duration of 700 h (Fig. 3(c)), owing to the confined environment that impedes the aggregation of Co particles. Hence, the Z@C@Z-P might be a more interesting candidate for CO_2 hydrogenation for its excellent stability.

To demonstrate the stability of the catalysts, the particles in the reduced and used catalysts are analyzed using STEM and EDX techniques. Figures 4(a)–4(d) illustrates that the average size of Co particles in the reduced Co_3O_4/ZnO is 22.1 nm (Figs. 4(a) and 4(b)), which increases to 31.7 nm after reaction (Figs. 4(c) and 4(d)), indicating that the deactivation can be attributed to a reduction in active sites resulting from particle agglomeration (Fig. 4(e)). For the Z@C-P sample, the average size of Co particles in the reduced catalyst is 34.1 nm (Figs. 4(f)) and 4(g)). After reaction for 140 h, some particles agglomerate into larger clusters, reaching sizes of approximately 70 nm, with the average size of Co particles increases to 48.6 nm (Figs. 4(h)–4(j)).

The Co particles in Z@C@Z-P remain within the ZnO interlayers after reduction (Figs. 4(k) and 4(l)). This is also verified by the nitrogen adsorption-desorption measurement, which indicates a slight increase of surface area (from 31.5 to 35.7 $m^2 \cdot g^{-1}$) and a similar type H3 hysteresis loop (Fig. S16 in the ESM). Hence, it is inferred that the peripheral ZnO layers remain intact, while the internal Co species experience lattice shrinkage due to partial reduction. After undergoing a reaction at 250 °C for 700 h, most of the Co particles remain in the ZnO interlayer, with only a small portion migrating to the outer surface of the ZnO layer (Figs. 4(m)–4(o)). From the large-scale STEM images and EDX mappings of the used Z@C@Z-P, it is evident that, even after being operated for 700 h, the Co particles remain well-dispersed (Fig. S17 in the ESM). This demonstrates that the confined space effectively prevents the migration and sintering of Co particles.

3 Conclusions

In summary, we report a lattice matching strategy to confine Co particles within the ZnO interlayers, through the continuous epitaxial growth of w-CoO over ZnO, or vice versa. The confined structure can also be achieved on ZnO with varied (e.g., rod) morphologies, and the Co loading within the catalyst can be precisely regulated by adjusting the amount of Co precursor added during the preparation process. Because of the epitaxial growth of CoO in the ZnO interlayers, the migration and agglomeration of the reduced Co particles formed in Z@C@Z-P can be effectively suppressed, thereby enhancing the stability of Co active sites for CO_2 hydrogenation reaction. Our findings offer a novel approach for the design of confined catalysts.

Electronic Supplementary Material: Supplementary material (experimental details, Figs. S1–S17, including STEM image, HRTEM image, EDX mapping images, XRD patterns, XPS spectra, TPR profiles, N_2 adsorption–desorption curve, and Tables S1–S5) is available in the online version of this article at https://doi.org/10.26599/NR.2025.94907282.

Data availability

All data needed to support the conclusions in the paper are presented in the manuscript and the ESM. Additional data related to this paper may be requested from the corresponding author upon request.

Acknowledgements

This work was supported by the National Natural Science Foundation of China (Nos. 42277485, 21976141, and 22102220), the Department of Science and Technology of Hubei Province (No. 2021CFA034), the Department of Education of Hubei Province (No. T2020011), and the State Key Laboratory of Pulp and Paper Engineering (No. 202301). S. A.C. C. acknowledges Fundação para a Ciência e Tecnologia and Ministério da Ciência, Tecnologia e Ensino Superior, Portugal (DOIs: 10.54499/LA/P/0008/2020, 10.54499/UIDP/50006/2020, 10.54499/UIDB/50006/2020, and 10.54499/CEECINST/00102/2018/CP1567/CT0026).

Declaration of competing interest

All the contributing authors report no conflict of interests in this work.

Author contribution statement

J. J. Z. and S. A.C. C.: Supervision, writing – review & editing, funding acquisition. S. L.: Conceptualization, data curation,

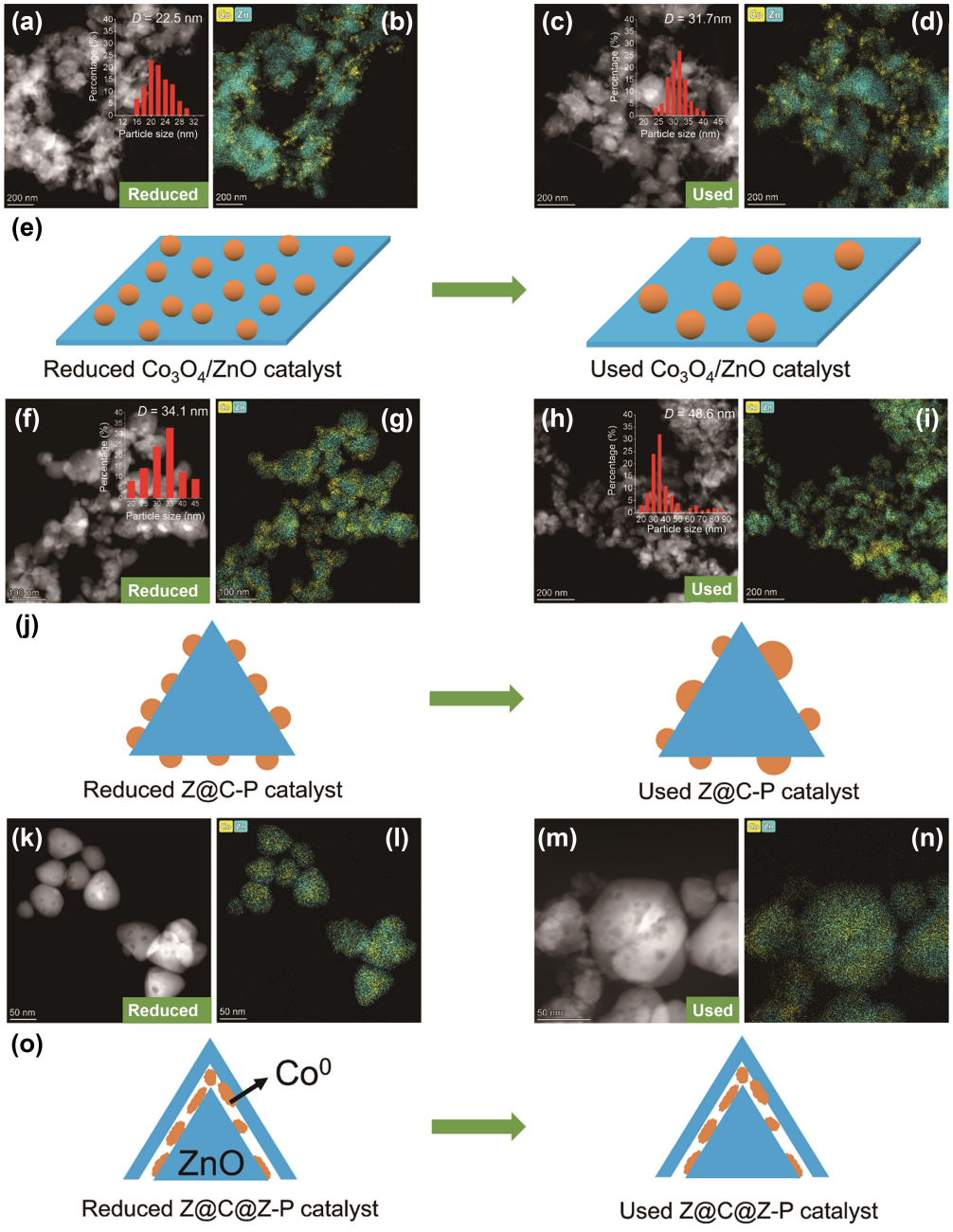

Figure 4 STEM image and corresponding EDX mapping of (a) and (b) the reduced Co_3O_4/ZnO catalyst and (c) and (d) the used Co_3O_4/ZnO catalyst. (e) Diagram illustrating the evolution of the Co_3O_4/ZnO catalyst during the reaction. STEM image and corresponding EDX mapping of (f) and (g) the reduced Z@C-P catalyst and (h) and (i) the used Z@C-P catalyst. (j) Diagram illustrating the evolution of the Z@C-P catalyst during the reaction. STEM image and corresponding EDX mapping of (k) and (l) the reduced Z@C@Z-P catalyst and (m) and (n) the used Z@C@Z-P catalyst. (o) Diagram illustrating the evolution of the Z@C@Z-P catalyst during the reaction. Reaction conditions: T = 250 °C, P = 2.0 MPa, GHSV = 6 $L \cdot h^{-1} \cdot g_{cat}^{-1}$, $H_2/CO_2/N_2$ = 67.5%/22.5%/10%. Reduction conditions: 300 °C in H_2 atmosphere for 3 h.

investigation, methodology, software, validation, writing original draft. W. X. Z., Y. L., W. W. X., Z. A. Z., and Z. Y. H.: Data curation, software, investigation. All the authors discussed the results and assisted during the manuscript preparation.

Use of AI statement

None.

References

[1] Fu, Q.; Li, W. X.; Yao, Y. X.; Liu, H. Y.; Su, H. Y.; Ma, D.; Gu, X. K.; Chen, L. M.; Wang, Z.; Zhang, H. et al. Interface-confined ferrous centers for catalytic oxidation. *Science* **2010**, *328*, 1141–1144.

[2] Leenders, S. H. A. M.; Gramage-Doria, R.; de Bruin, B.; Reek, J. N. H. Transition metal catalysis in confined spaces. *Chem. Soc. Rev.* **2015**, *44*, 433–448.

[3] Gao, C. B.; Lyu, F. L.; Yin, Y. D. Encapsulated metal nanoparticles for catalysis. *Chem. Rev.* **2021**, *121*, 834–881.

[4] Grommet, A. B.; Feller, M.; Klajn, R. Chemical reactivity under nanoconfinement. *Nat. Nanotechnol.* **2020**, *15*, 256–271.

[5] Wang, N.; Sun, Q. M.; Yu, J. H. Ultrasmall metal nanoparticles confined within crystalline nanoporous materials: A fascinating class of nanocatalysts. *Adv. Mater.* **2019**, *31*, 1803966.

[6] Chai, Y. C.; Wu, G. J.; Liu, X. Y.; Ren, Y. J.; Dai, W. L.; Wang, C. M.; Xie, Z. K.; Guan, N. J.; Li, L. D. Acetylene-selective hydrogenation catalyzed by cationic nickel confined in zeolite. *J. Am. Chem. Soc.* **2019**, *141*, 9920–9927.
[7] Ding, W.; Wei, Z. D.; Chen, S. G.; Qi, X. Q.; Yang, T.; Hu, J. S.; Wang, D.; Wan, L. J.; Alvi, S. F.; Li, L. Space-confinement-induced synthesis of pyridinic- and pyrrolic-nitrogen-doped graphene for the catalysis of oxygen reduction. *Angew. Chem., Int. Ed.* **2013**, *52*, 11755–11759.
[8] Sanlés-Sobrido, M.; Pérez-Lorenzo, M.; Rodríguez-González, B.; Salgueiriño, V.; Correa-Duarte, M. A. Highly active nanoreactors: Nanomaterial encapsulation based on confined catalysis. *Angew. Chem., Int. Ed.* **2012**, *51*, 3877–3882.
[9] Wang, N.; Sun, Q. M.; Bai, R. S.; Li, X.; Guo, G. Q.; Yu, J. H. *In situ* confinement of ultrasmall Pd clusters within nanosized silicalite-1 zeolite for highly efficient catalysis of hydrogen generation. *J. Am. Chem. Soc.* **2016**, *138*, 7484–7487.
[10] Pan, X. L.; Bao, X. H. Reactions over catalysts confined in carbon nanotubes. *Chem. Commun*. **2008**, 6271–6281.
[11] Pan, X. L.; Fan, Z. L.; Chen, W.; Ding, Y. J.; Luo, H. Y.; Bao, X. H. Enhanced ethanol production inside carbon-nanotube reactors containing catalytic particles. *Nat. Mater.* **2007**, *6*, 507–511.
[12] Guan, J.; Pan, X. L.; Liu, X.; Bao, X. H. Syngas segregation induced by confinement in carbon nanotubes: A combined first-principles and Monte Carlo study. *J. Phys. Chem. C* **2009**, *113*, 21687–21692.
[13] Abbaslou, R. M. M.; Tavassoli, A.; Soltan, J.; Dalai, A. K. Iron catalysts supported on carbon nanotubes for Fischer-Tropsch synthesis: Effect of catalytic site position. *Appl. Catal. A: Gen.* **2009**, *367*, 47–52.
[14] Shifa, T. A.; Vomiero, A. Confined catalysis: Progress and prospects in energy conversion. *Adv. Energy Mater.* **2019**, *9*, 1902307.
[15] Tessonnier, J. P.; Ersen, O.; Weinberg, G.; Pham-Huu, C.; Su, D. S.; Schlögl, R. Selective deposition of metal nanoparticles inside or outside multiwalled carbon nanotubes. *ACS Nano* **2009**, *3*, 2081–2089.
[16] Gao, Z.; Qin, Y. Design and properties of confined nanocatalysts by atomic layer deposition. *Acc. Chem. Res.* **2017**, *50*, 2309–2316.
[17] Xia, Y. N.; Gilroy, K. D.; Peng, H. C.; Xia, X. H. Seed-mediated growth of colloidal metal nanocrystals. *Angew. Chem., Int. Ed.* **2017**, *56*, 60–95.
[18] Liu, J.; Zhang, J. T. Nanointerface chemistry: Lattice-mismatch-directed synthesis and application of hybrid nanocrystals. *Chem. Rev.* **2020**, *120*, 2123–2170.
[19] Lyu, S.; Wang, S.; He, Z. Y.; Yang, J.; Xu, X.; Carabineiro, S. A. C.; Zhu, J. J. Lattice matching strategy to construct highly active hcp-Co phase for Fischer-Tropsch synthesis. *ACS Mater. Lett.* **2024**, *6*, 856–864.
[20] Seo, W. S.; Shim, J. H.; Oh, S. J.; Lee, E. K.; Hur, N. H.; Park, J. T. Phase- and size-controlled synthesis of hexagonal and cubic CoO nanocrystals. *J. Am. Chem. Soc.* **2005**, *127*, 6188–6189.
[21] Qi, J. B.; Hu, X. The loss of ZnO as the support for metal catalysts by H_2 reduction. *Phys. Chem. Chem. Phys.* **2020**, *22*, 3953–3958.
[22] Peng, Z. A.; Peng, X. G. Mechanisms of the shape evolution of CdSe nanocrystals. *J. Am. Chem. Soc.* **2001**, *123*, 1389–1395.
[23] Zhang, Y. H.; Liu, X. Y.; Li, Z.; Lyu, S.; Zhou, Y. Y.; Long, Y. H.; Li, J. L.; Wang, L. Nano-bricks assembly toward 1D metal oxide nanorods. *Small* **2024**, *20*, 2304944.
[24] Sheng, Z. T.; Lyu, S.; Liu, X. Y.; Zhang, Y. H.; Li, J. L.; Zhu, J. J.; Carabineiro, S. A. C. Designing multielement nanointerfaces in supported catalysts by ultra small lattice mismatch. *Appl. Surf. Sci.* **2024**, *646*, 158918.
[25] Li, G. R.; Hu, T.; Pan, G. L.; Yan, T. Y.; Gao, X. P.; Zhu, H. Y. Morphology-function relationship of ZnO: Polar planes, oxygen vacancies, and activity. *J. Phys. Chem. C* **2008**, *112*, 11859–11864.
[26] McLaren, A.; Valdes-Solis, T.; Li, G. Q.; Tsang, S. C. Shape and size effects of ZnO nanocrystals on photocatalytic activity. *J. Am. Chem. Soc.* **2009**, *131*, 12540–12541.
[27] ten Have, I. C.; Kromwijk, J. J. G.; Monai, M.; Ferri, D.; Sterk, E. B.; Meirer, F.; Weckhuysen, B. M. Uncovering the reaction mechanism behind CoO as active phase for CO_2 hydrogenation. *Nat. Commun.* **2022**, *13*, 324.
[28] Ji, Y. G.; Zhao, Z.; Duan, A. J.; Jiang, G. Y.; Liu, J. Comparative study on the formation and reduction of bulk and Al_2O_3-supported cobalt oxides by H_2-TPR technique. *J. Phys. Chem. C* **2009**, *113*, 7186–7199.
[29] Griffin, G. L.; Yates, J. T. Jr. Combined temperature-programmed desorption and infrared study of H_2 chemisorption on ZnO. *J. Catal.* **1982**, *73*, 396–405.
[30] Anderson, A. B.; Nichols, J. A. Hydrogen on zinc oxide. *Theory of its heterolytic adsorption. J. Am. Chem. Soc.* **1986**, *108*, 4742–4746.
[31] Dong, C.; Mu, R. T.; Li, R. T.; Wang, J. Y.; Song, T. Y.; Qu, Z. P.; Fu, Q.; Bao, X. H. Disentangling local interfacial confinement and remote spillover effects in oxide-oxide interactions. *J. Am. Chem. Soc.* **2023**, *145*, 17056–17065.
[32] Lyu, S.; Wu, Q. S.; Li, Z.; Zhang, Y. H.; Li, J. L.; Wang, L. Cobalt clusters decorated $Co_xMn_{1-x}O$ nanocomposites for improving the efficiency of syngas to lower olefins with lower CO_2 emission. *Appl. Catal. B: Environ.* **2023**, *325*, 122347.